SUPPORTING INFORMATION

Stress-Induced Variations in the Stiffness of Micro- and Nano-Cantilever Beams

R. B. Karabalin[1], L. G. Villanueva[1], M. H. Matheny[1], J. E. Sader[2], M. L. Roukes[1]
[1]*Kavli Nanoscience Institute, California Institute of Technology, Pasadena, California 91125,*
[2]*Department of Mathematics and Statistics, The University of Melbourne, Victoria 3010, Australia*

I. Effect of Surface Stress on Doubly-Clamped Beams

A. Axial force model (Stress effect in Table I)

In this section, we derive the required formulas for the effect of surface stress on the resonant frequency of doubly-clamped beams due to the axial tension built up along the beam (*stress effect* in Table I). In the main manuscript we discussed that a net axial force is induced in doubly-clamped beams, along their major axis. This net axial force is given by the integral of the resulting axial stress over the beam cross-section. For the resonators used here, this coincides with the integral of the axial stress in the active piezoelectric layer only; other parts of the beam do not contribute to the net axial force because the beam-ends are restrained from moving. The net axial force determines the resulting effect on resonance frequency and/or stiffness of the device.

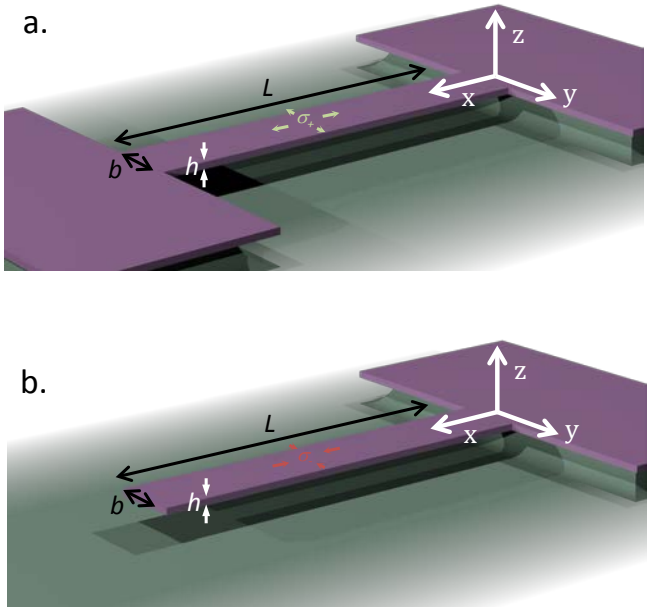

Figure S1 | Graphical representation of a doubly-clamped (a) and a cantilever (b) beam with the dimensions used in the paper, as well as the axis definition. In (a) a compressive stress (positive stress by convention) is shown, whereas in (b) a tensile (negative by convention) stress is shown.

The effect of surface stress on the resonance frequency of a doubly-clamped beam is calculated to leading order for small surface stress loads, and thus gives a linear relationship between the resonant frequency shift and the applied surface stress change. It is assumed that the beam structure possesses a rectangular cross-section whose width b greatly exceeds its thickness h, i.e., the beam is formally a thin plate[S1]. The length of the structure is L (see Fig. S1).

We use the general theoretical formalism presented elsewhere[S2] to calculate the effect of surface stress, and thus decompose the problem into two subproblems:

Subproblem (1): Deformation of an unrestrained plate under application of a net surface stress load.

Subproblem (2): Beam structure with no surface stress load and a specified in-plane displacement to satisfy the required clamped boundary conditions at the ends.

Superposition of these two subproblems gives the required in-plane deformation of the original problem, with exact satisfaction of free edge and clamped boundary conditions; see ref. S2 for details.

Application of a net surface stress change to the surface of the structure, with the clamped boundary conditions removed, results in an isotropic strain whose displacement field is:

$$(u,v) = -\frac{(1-\nu)\sigma_s^T}{Eh}(x,y) \ , \tag{S1}$$

where u and v are displacements in the x and y directions, respectively; (x,y) are the Cartesian coordinates in the plane (see Fig. S1); ν and E are the Poisson ratio and Young's modulus of beams material respectively; h is the device thickness; and σ_s^T is the total applied surface stress[S2]. This is the required solution to Subproblem (1).

To account for the clamped displacement conditions at the end of the structure, in accord with Subproblem (2), a displacement load in the x-direction must be applied to its ends; displacements in the y-direction are not important since the beam length greatly exceeds its width, in accord with Saint-Venant's principle[S3]. From Eq. (S1), this axial displacement is:

$$u = \frac{(1-\nu)\sigma_s^T L}{Eh} \ , \tag{S2}$$

where L is the beam length. Such an axial displacement induces an axial tensile load:

$$F_{axial} = (1-\nu)\sigma_s^T b \ , \tag{S3}$$

where b is the beam width. The axial load in Eq. (S3) will lead to a change in stiffness and hence resonant frequency. Since the beam length greatly exceeds width and thickness, this effect is calculated from Euler-Bernoulli beam theory. The governing equation for the deflection function w, for a beam of linear mass density μ and areal moment of inertia I, is:

$$EI\frac{\partial^4 w}{\partial x^4} - F_{axial}\frac{\partial^2 w}{\partial x^2} + \mu\frac{\partial^2 w}{\partial t^2} = 0 \ , \tag{S4}$$

which is solved with the usual clamped boundary conditions at the beam ends, $w = w' = 0$.

We assume an explicit time dependence of $\exp(-i\omega t)$, where ω is the angular frequency and t is time, i.e., $w(x,t) = W(x)\exp(-i\omega t)$. Multiplying both sides of Eq. (S4) by the deflection function w, scaling x by the beam length L, and integrating over the beam length yields the following exact result for square of the radial resonant frequency:

$$\omega^2 = \frac{EI}{L^4\mu}\left(\frac{\int_0^1 (W''(\bar{x}))^2 d\bar{x}}{\int_0^1 (W(\bar{x}))^2 d\bar{x}} + \frac{F_{axial}L^2}{EI}\frac{\int_0^1 (W'(\bar{x}))^2 d\bar{x}}{\int_0^1 (W(\bar{x}))^2 d\bar{x}}\right), \tag{S5}$$

where $\bar{x} = \dfrac{x}{L}$ is the scaled axial distance.

To calculate the leading order effect of surface stress change on the frequency shift, we use the deflection function for a doubly-clamped beam in the absence of surface stress. Solving Eq. (S4) under this condition then gives:

$$W(\bar{x}) = \cosh D_n\bar{x} - \cos D_n\bar{x} + \frac{\cosh D_n - \cos D_n}{\sinh D_n - \sin D_n}\left(\sin D_n\bar{x} - \sinh D_n\bar{x}\right) \ , \tag{S6}$$

where D_n is the n-th positive root of:

$$\cosh D_n \cos D_n = 1, \tag{S7}$$

with $n = 1$ corresponding to the fundamental mode.

Substituting Eq. (S6) with $n = 1$ into Eq. (S5), and using Eq. (S3), then yields the required result:

$$\frac{\Delta\omega}{\omega_R} = 0.1475\frac{(1-\nu)\sigma_s^T}{Eh}\left(\frac{L}{h}\right)^2, \tag{S8}$$

where the original radial resonance frequency $\omega_R = 2\pi f_R = 6.459h/L^2\sqrt{E/\rho}$, the beam mass density is ρ, and the radial frequency shift is defined $\Delta\omega = \omega - \omega_R$. We emphasize that Eq. (S8) is valid in the asymptotic limit of small stress loads. An alternate derivation of this formula is given in Ref. S4.

B. Change in dimensions (Geometric Effect in Table I)

Due to the boundary conditions in a doubly-clamped beam, after an isotropic in-plane stress is applied to the beam the strain map that develops is:

$$\varepsilon_{xx} = 0; \varepsilon_{yy} = (1+\nu)\frac{(1-\nu)\sigma_s^T}{Eh}; \varepsilon_{zz} = \frac{\nu(1+\nu)}{1-\nu}\frac{(1-\nu)\sigma_s^T}{Eh} \tag{S9}$$

Assuming that the Young's modulus of the material remains unchanged during the application of stress, the relative change in the resonant frequency would be:

$$\frac{\Delta\omega}{\omega_R} = -\frac{1}{2}\frac{\Delta\rho}{\rho} + \frac{\Delta t}{t} - 2\frac{\Delta L}{L} = \frac{1}{2}\frac{\Delta \mathrm{V}}{V} + \frac{\Delta t}{t} - 2\frac{\Delta L}{L} \approx -\frac{3}{2}\varepsilon_{xx} + \frac{1}{2}\varepsilon_{yy} + \frac{3}{2}\varepsilon_{zz} \tag{S10}$$

That, using (S9) with (S10), yields:

$$\frac{\Delta\omega}{\omega_R} \approx \frac{(1+\nu)(1+2\nu)}{1-\nu}\frac{(1-\nu)\sigma_s^T}{Eh} \tag{S11}$$

which is the expression found in Table I in the main manuscript. In the case of doubly-clamped beams and the typical geometries that are used $\left(\frac{L}{h} >> 1\right)$, the *stress effect* described previously is much larger than this *geometric effect*.

II. (Unphysical) Axial Force Model for Cantilever Beams

It has been widely assumed that application of surface stress to a cantilever beam induces an axial force along the beam length. This so-called "axial force model" has been shown to be unphysical and in violation of Newton's 3rd law[S2,S5,S6]. For completeness, however, we reproduce the resulting formula derived from this model[S7]. This allows comparison and assessment with measurements performed in this study.

In the limit of small surface stress loads, the axial force model has been reported under various forms[S7-12]. Since the underlying model is unphysical, we refrain from any discussion on the merits of each form and simply report the most common formula that has been claimed to yield good agreement with measurements[S7]:

$$\frac{\Delta\omega}{\omega_R} = \frac{12}{\pi^2}\frac{\sigma_s^T}{Eh}\left(\frac{L}{b}\right)\left(\frac{L}{h}\right)^2 \approx 1.2\frac{\sigma_s^T}{Eh}\left(\frac{L}{b}\right)\left(\frac{L}{h}\right)^2. \tag{S12}$$

Comparing this result with the (physically correct) model for doubly-clamped beams in Eq. (S8), we observe that the axial force model predicts a larger shift in frequency in cantilever beams than in doubly-clamped beams, by a factor of:

$$\left.\frac{\Delta\omega}{\omega_R}\right|_{cant} \Big/ \left.\frac{\Delta\omega}{\omega_R}\right|_{beam} = \frac{8}{(1-\nu)}\frac{L}{b}. \tag{S13}$$

Since $L/b >> 1$, the axial force model predicts that cantilever beams are much more sensitive to surface stress changes than doubly-clamped beams. This is not observed in the controlled measurements of doubly-clamped and cantilever beams reported in this study.

III. Piezoelectric loads in doubly-clamped beams

The piezoelectric effect couples the mechanical and electrical degrees of freedom of a material by the following relation

$$(\varepsilon) = [C]\cdot(\sigma) + [d]\cdot(E) \tag{S14}$$

where (ε) and (σ) are the mechanical strain and stress vectors, respectively; $[C]$ is the compliance matrix of the material, (E) is the electric field vector and $[d]$ is the piezoelectric matrix, which is directly responsible for the mechanical/electrical coupling. For the piezoelectric material considered in this study, the piezoelectric matrix is of the form (with axis 1, 2 and 3 pointing along the beam, transversal in-plane and out-of-plane respectively):

$$[d] = \begin{bmatrix} 0 & 0 & d_{31} \\ 0 & 0 & d_{31} \\ d_{31} & d_{31} & d_{33} \\ 0 & d_{45} & 0 \\ d_{45} & 0 & 0 \\ 0 & 0 & 0 \end{bmatrix}. \tag{S15}$$

The application of an external voltage between two electrodes contacting the piezoelectric material (as in our experimental case) leads to the generation of an electric field and, consequently, deformation of the material. Following a similar approach to that taken in Section I of the SI, we first calculate the deformation of the unrestrained piezoelectric material. This allows the material to expand or contract freely and therefore the in-plane strains ε_{xx} along the beam and ε_{yy} perpendicular to the beam and out-of-plane strain ε_{zz} are given by:

$$\varepsilon_{xx} = \varepsilon_{yy} = -d_{31}\frac{V}{h_{PZE}}; \quad \varepsilon_{zz} = -d_{33}\frac{V}{h_{PZE}}, \tag{S16}$$

where V is the applied voltage and h_{PZE} is the thickness of the piezoelectric layer.

However, the composite beam structure used in the present devices contains other materials that are not piezoelectric. Those materials impose some restrictions on the total deformation, which will be a combination of net elongation and bending. As a first approximation, bending does not contribute to the stiffness of the beam[S2] and therefore we can limit our analysis to the net (average) strain. This net strain is given by Eq. (S17) when the Poisson ratios of the different materials are identical (which is an excellent approximation in the present case):

$$\left\langle \varepsilon_{xx} \right\rangle = \left\langle \varepsilon_{yy} \right\rangle = -d_{31} \frac{E_{PZE}}{\sum E_i h_i} V; \quad \left\langle \varepsilon_{zz} \right\rangle = -d_{33} \frac{V}{h_{tot}} \tag{S17}$$

where E_{PZE} is the Young's modulus of the piezoelectric material, h_{tot} is the total thickness of the beam, and the summation in the denominator extends to all four layers of the composite structure, with E_i and h_i being the Young's modulus and thickness of every layer, respectively. The brackets in equation (S17), $\left\langle \varepsilon_{ii} \right\rangle$, mean average over the cross section of the beam (*y*-*z* plane).

Following the approach of Section I of the SI, we initially consider the case of a doubly-clamped beam. The solution above corresponds to Subproblem (2) in Section I. Subproblem (2) then requires a displacement load in the *x*-direction to match the required clamped boundary conditions at the beam ends, as discussed above. This axial displacement induces the following axial load:

$$F_{axial} = d_{31} E_{PZE} V b \ . \tag{S18}$$

Equation (S18) can now be directly compared to Eq. (S3) and the derivation performed in Section I is valid here. We can thus write an expression equivalent to (S8), in this case for a piezoelectric beam:

$$\frac{\Delta\omega}{\omega_R} = 0.0123 \, d_{31} V \frac{E_{PZE}}{\langle EI \rangle} b L^2 , \tag{S19}$$

where <*EI*> is the effective flexural rigidity of the beam. If the Young's moduli of the different materials in the composite structure are approximately the same, Eq. (S19) immediately leads to:

$$\frac{\Delta\omega}{\omega_R} = 0.1475 \ \frac{d_{31} V}{h_{tot}} \left(\frac{L}{h_{tot}} \right)^2 , \tag{S20}$$

which is only dependent on total thickness h_{tot}. Comparing Equations (S8) and (S20), it is evident that the effects of an applied voltage are equivalent to the effects of an applied surface stress, as required. This leads to the following relation connecting an equivalent surface stress to a given applied voltage:

$$\sigma_s^T = d_{31} \frac{E}{(1-\nu)} V \ . \tag{S21}$$

Note that in the calculation of the change in frequency for a doubly-clamped beam, we have neglected any differential change in dimensions, since this is much smaller than the contribution given by Eq. (S20) (we assume that any beam holds the condition $L > h_{tot}$).

IV. Cantilever beams

A. Isotropic material – surface stress load

We begin by considering a cantilever plate composed of an isotropic material under a surface stress load – this effect is due to surface stress change; see ref. S2.

The *in-plane stress* effect has been analyzed previously and yields[S2]:

$$\frac{\Delta\omega}{\omega_R} = \phi(\nu)\frac{(1-\nu)\sigma_s^T}{Eh}\left(\frac{b}{L}\right)\left(\frac{b}{h}\right)^2, \tag{S22}$$

where numerical coefficient $\phi(\nu) \approx -0.042\nu$ is estimated via FEM and accounts for 3D effects of the stress distribution close to the clamp. A detail exposition of the derivation of this formula and its physical features is given in Ref. S4.

The *geometric* effect is given by the differential change in dimensions of the cantilever beam, due to the surface stress load. This tunes the stiffness and the resonant frequency of the cantilever, and yields (considering $\varepsilon_{xx} = \varepsilon_{yy}$):

$$\frac{\Delta\omega}{\omega_R} = -\frac{1}{2}\frac{\Delta\rho}{\rho} + \frac{\Delta h}{h} - 2\frac{\Delta L}{L} = \frac{3}{2}\varepsilon_{zz} - \varepsilon_{xx} = \frac{(1+2\nu)\sigma_s^T}{Eh}, \tag{S23}$$

In the limit as $h/b \to 0$ (commensurate with the assumptions of thin plate theory[S2]), the in-plane stress contribution in Eq. (S22) dominates the geometric effect in Eq. (S23), for large and fixed aspect ratio L/b. The in-plane stress effect remains prevalent for thin beams under the condition:

$$\frac{b}{h} < \left.\frac{b}{h}\right|_{\text{critical}} \approx 5\sqrt{\frac{1+2\nu}{\nu(1-\nu)}\frac{L}{b}}, \tag{S24}$$

whereas for thicker beams, the geometric effect will dominate.

These results are gathered in Table I of the main manuscript.

B. Piezoelectric material – voltage load

For the piezoelectric beams used in this study, the geometric effect can also be calculated:

$$\frac{\Delta\omega}{\omega_R} = -\frac{1}{2}\frac{\Delta\rho}{\rho} + \frac{\Delta h}{h} - 2\frac{\Delta L}{L} = \frac{3}{2}\left\langle \varepsilon_{zz} \right\rangle - \left\langle \varepsilon_{xx} \right\rangle = \left(-\frac{3}{2}\frac{d_{33}}{h_{tot}} + \frac{d_{31}}{h_{tot}} \right) V \,. \tag{S27}$$

The changes in the Young's modulus and Poisson ratio of the materials are neglected. For the piezoelectric material used here, $d_{33} = -2d_{31}$, and hence Eq. (S27) becomes:

$$\frac{\Delta\omega}{\omega_R} = 4\frac{d_{31}}{h_{tot}} V \,. \tag{S28}$$

Calculation of the stress effect in the devices considered is complicated by the multilayer structure of the piezoelectric cantilevers, and their non-isotropic material properties. Three-dimensional FEM analysis is thus used to obtain the combined contributions of stress and geometric effects, complementing Eq. (S28). This total effect is plotted in Fig. 3. We find that the geometric effect dominates the results.

V. Measurement of NEMS Device Response

We employ an optical interferometric detection scheme to sense the mechanical motion of our NEMS devices[S13]. This detection mechanism is used due to ease of implementation, high mechanical responsivity to out-of-plane beam displacements and negligible RF background noise.

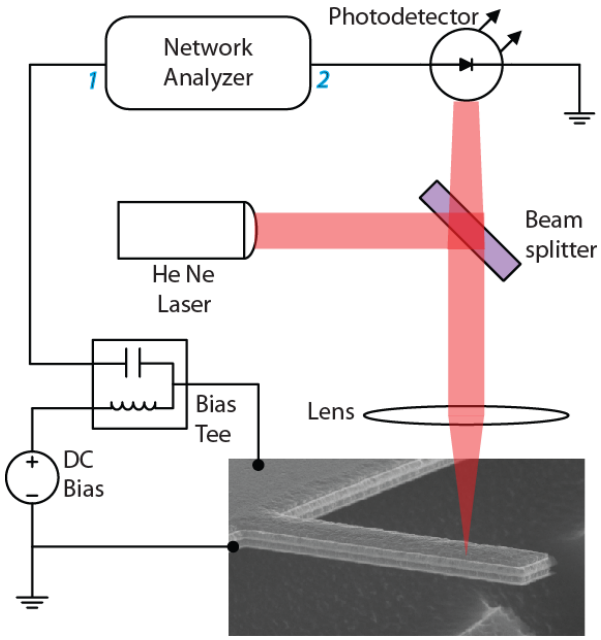

Figure S2 | Schematic of the optical interferometric detection setup used for sensing the motion of NEMS devices

A schematic of the experimental setup is shown in Fig. S2. The devices are mounted in a custom-built room temperature vacuum chamber fitted with a quartz optical window for interrogation. An optical cavity is created between a two-mirror system formed by the bottom of the substrate and the top surface of the NEMS device. The light source consists of a regular helium neon laser (λ = 632 nm) followed by a beam expander and an attenuator. After the original laser beam passes the beam splitter oriented at 45^{o}, one component is focused onto the NEMS device with a lens of 0.15 numerical aperture, resulting in a spot size ~10–20 μm. Interference between laser beams reflected from the top surface of the mechanical resonator and bottom substrate is detected using a high-bandwidth low-noise photodetector. As a result, the resonator motion modulates the light intensity in proportion to the magnitude of the mechanical displacement.

An AC voltage between top and bottom electrodes of the NEMS device actuates the out-of-plane motion, while a DC bias produces the required external stress studied in this work. Both voltages are combined using a bias-tee. A vector network analyzer is used to measure the resonance spectral response of the resulting signal. To perform the frequency shift experiments, the network analyzer operates in a continuous wave (CW) regime and is controlled by an external computer that is used to provide phase locked loop (PLL) operation.

A slight asymmetry between tunability slopes is observed in doubly clamped beams. We attribute this to an electrostatic effect from the substrate that affects the resonant frequency as V^2. When fitting the experimental data to a second-degree polynomial, the fit is more accurate but the linear slope, nevertheless, remains the same (relative change smaller than 1%). In subsequent experiments, we used a wafer with a thick sacrificial silicon oxide layer underneath the seed aluminum nitride layer and this reduced by two orders of magnitude the coefficient of second order in the polynomial. In this case, again, the linear slope remains the same. We therefore believe that the conclusions drawn in the current paper are not affected by the observed small symmetry-breaking.

Fig. 3 in the main manuscript also shows some apparent asymmetry and, in addition, an apparent discrepancy of the scaling with $1/L^2$. In order to clarify this issue, we replot Fig. 3 from the main manuscript as Fig. S3, in this case with error bars. The error bars for the experimental data are calculated based on the measured Allan Deviation of $5 \cdot 10^{-6}$, representing the 95% confidence bounds. The error bars for the FEM data correspond to the typical expected accuracy of FEM simulations, accounting for geometrical and material uncertainties and convergence of the frequency shift; see Section VI-A. The discrepancy between theoretical prediction and measurement slopes is on the order of ~5-15%. This is a reasonable agreement considering the shown experimental error of ~10%, especially visible on scaled plot shown in Fig S3(a). Therefore, the slight asymmetry and discrepancy with the scaling appear both to be negligible, when careful analysis of measurement errors is taken into account.

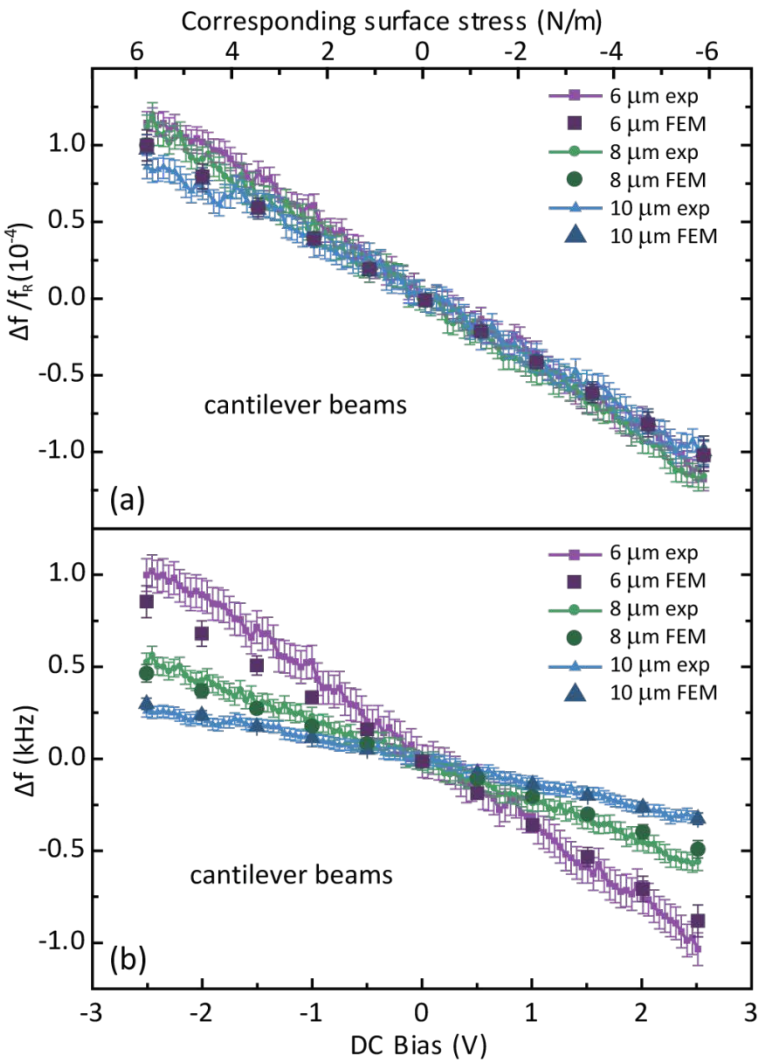

Figure S3 | (a) Relative $\Delta f/f_R$ and **(b)** absolute Δf frequency shift for three cantilevers (Fig. 3 in the main manuscript) with error bars. The experimental uncertainties show 95% confidence bounds and they are calculated based on the observed Allan Deviation of $5{\cdot}10^{-6}$ – a measure of cantilevers' frequency fluctuations. The error bars for FEM data are based on estimated geometrical and material uncertainties and convergence of the frequency shift (see Section VI-A).

VI. Finite Element Simulations

Extensive Finite Element Method (FEM) simulations have been performed to (i) compare with experimental results on piezoelectric beams, and (ii) assess theoretical predictions from the presented models for uniform beams. In all the cases, the objective of the simulations was to compute the frequency shift caused by an applied load, which could be either stress (in a uniform beam) or transverse applied electric field in the piezoelectric material.

A commercial software was used to perform these simulations. The methodology used consists of performing first a static analysis of the system with the applied load, allowing the system to respond to this load. Subsequently, a modal analysis is performed using the resulting stresses/strains from the static analysis. This modal analysis can account individually for the effect of structural stress on the resulting stiffness, and/or for the effect of the resulting strain on the geometric change in dimensions.

A. Mesh convergence

The utilized mesh is refined until 99% convergence in the interesting magnitudes is achieved. Convergence is defined, for the static analysis, by monitoring the maximum strain, stress and deformation, observing that all of them converge at about the same rate. In the case of modal analysis, convergence is defined by monitoring the frequency of the first out of plane flexural vibrational mode. The mesh refinement converges at the same size for both modal and static analysis.

The convergence of the simulated frequency shift was also studied. In the case of doubly-clamped beams, the frequency shift due to stress can be observed to converge at the same rate as the frequency. However, when considering the stress effect in cantilever beams or the geometric effect for either of both types of beams, the frequency shift cannot be converged better than 95%. This is most likely due to the property that the frequency shift is much smaller in these cases and the number is so small that, as soon as the mesh refines, it also introduces numerical uncertainty that is of the order of 5% of the frequency shift. We therefore make all the simulations considering a 99% convergence in frequency shift for the stress effect in doubly-clamped beams and a 95% convergence in frequency shift for remaining cases.

B. Piezoelectric devices

Cantilever and doubly-clamped beams are simulated in accord with the geometry and clamping conditions of the fabricated devices. This includes a small ledge in the anchoring region, which is found to be necessary for better comparison between experiments and simulations (bringing them about 2-4% closer). The used material properties are: $E_{\mathrm{AlN}} = 345$ GPa, $\nu_{\mathrm{AlN}} = 0.3$, $\rho_{\mathrm{AlN}} = 3230$ kg/m^3, $d_{31,\mathrm{AlN}} = -2.5$ pm/V, $E_{\mathrm{Mo}} = 329$ GPa, $\nu_{\mathrm{Mo}} = 0.31$, $\rho_{\mathrm{Mo}} = 10.300$ kg/m^3. By changing the applied external voltage, simulations of the experimental measurements are produced, as shown in Fig. 2 and Fig. 3 of the main article. No change in Young's modulus and Poisson's ratio was considered during these simulations.

As introduced before, we perform independent simulations to account for each of both effects (stress and geometrical changes). In the latter case, we find a remarkable quantitative agreement for the frequency shift when comparing FEM results with the analytical predictions of Eq. (S28) (5% difference). The simulated/theoretically predicted frequency shift accounts for as much as 75% of the experimentally observed frequency shift.

Stress induced frequency shifts in piezoelectric cantilevers are larger than expected for uniform beams[S2]. Equation (S22) (with $\phi(\nu) \approx -0.042\nu$) predicts around 2% of the observed frequency shift, while FEM simulations represent around 20% of the experimentally observed frequency shift (which added to the geometrical effect described before corresponds to 95% of it). We attribute this divergence between FEM (and experimental results) and theory to the actual non-uniform geometry of the multi-layer resonators used experimentally. A possibility recently brought up in the literature[S14] could be the fact that our structure is not completely symmetric, but has some asymmetry due to the bottom AlN layer. FEM simulations disprove this explanation – when we remove the asymmetry, the results (relative frequency shifts) are not affected.

The simulations diverge from the experimental results by around 5%. In the case of the cantilever beams we attribute this to the limit in the accuracy of our technique. In the case of the doubly-clamped beams, the divergence is mostly caused by a deviation from linear behavior of the experimental results. The origin of this effect has not yet been elucidated but a plausible explanation can lie in variations of the Young's modulus due to the axial stress generated along the beam.

C. Uniform beam with surface stress load

To assess the validity of the theoretical model developed, simulations of cantilever and doubly-clamped beams composed of a single material were also performed. In this case, ideal anchoring was utilized, i.e. no ledge was included in the model. We use the following typical material properties: E = 200 GPa, ρ = 2000 kg/m^3. The Poisson's ratio of the material, ν, assumed the values ν = 0, 0.25, 0.49. Following the procedure described above, several simulations were performed by varying the applied load (in this case surface stress). The normalized frequency shift, Ω, was then determined:

$$\Omega = \left|\frac{\Delta\omega}{\omega_0}\right| \Big/ \left|(1-\nu)\frac{\sigma_s^T}{Eh}\left(\frac{b}{L}\right)\right| . \qquad \text{(S29)}$$

In Fig. S4, the normalized frequency shifts are plotted for different Poisson's ratios as a function of the ratio b/h, for a given L/b = 10. Contributions due to stress in the cantilever material and change in cantilever dimensions are shown separately in Fig. S4. They correspond precisely to the predictions of Eq. (S25) and Eq. (S26). Different crossover points of the contributions are found for different Poisson's ratios, also as predicted by Eq. (S24).

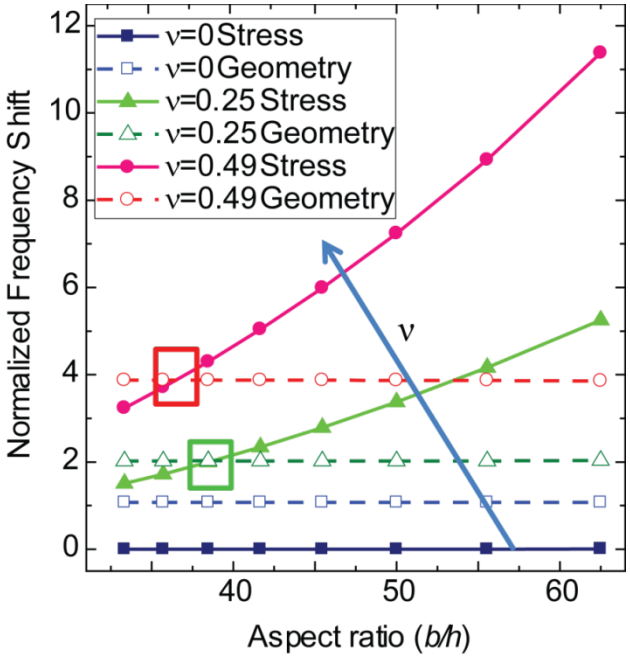

Figure S4 | FEM simulation results of relative contribution of stress (filled markers, solid line) and geometry (hollow markers, dashed line) on Ω. Results given as a function of ratio b/h for ν = 0, 0.25 and 0.49. The crossover regions are highlighted by large rectangles and are located at b/h ~ 35-40.

VII. References

S1. Timoshenko, S. & Woinowsky-Krieger, S., *Theory of plates and shells*. 2d ed. Engineering societies monographs. 1959, New York: McGraw-Hill. 580.

S2. Lachut, M.J. & Sader, J.E. Effect of surface stress on the stiffness of cantilever plates. *Phys. Rev. Lett.* **99,** 206102 (2007).

S3. Timoshenko, S. & Goodier, J.N., *Theory of elasticity*. 3d ed. Engineering societies monographs. 1969, New York,: McGraw-Hill. xxiv, 567 p.

S4. Lachut, M.J. & Sader, J.E. Effect of surface stress on the stiffness of thin elastic plates and beams. *Phys. Rev. B* **85,** 085440 (2012).

S5. Lu, P., Lee, H.P., Lu, C. & O'Shea, S.J. Surface stress effects on the resonance properties of cantilever sensors. *Phys. Rev. B* **72,** 085405 (2005).

S6. Gurtin, M.E., Markenscoff, X. & Thurston, R.N. Effect of Surface Stress on Natural Frequency of Thin Crystals. *Appl. Phys. Lett.* **29,** 529-530 (1976).

S7. McFarland, A.W., Poggi, M.A., Doyle, M.J., Bottomley, L.A. & Colton, J.S. Influence of surface stress on the resonance behavior of microcantilevers. *Appl. Phys. Lett.* **87,** 053505 (2005).

S8. Lagowski, J., Gatos, H.C. & Sproles, E.S. Surface Stress and Normal Mode of Vibration of Thin Crystals - Gaas. *Appl. Phys. Lett.* **26,** 493-495 (1975).

S9. Hwang, K.S., Eom, K., Lee, J.H., Chun, D.W., Cha, B.H., Yoon, D.S., Kim, T.S. & Park, J.H. Dominant surface stress driven by biomolecular interactions in the dynamical response of nanomechanical microcantilevers. *Appl. Phys. Lett.* **89,** 173905 (2006).

S10. Cherian, S. & Thundat, T. Determination of adsorption-induced variation in the spring constant of a microcantilever. *Appl. Phys. Lett.* **80,** 2219-2221 (2002).

S11. Chen, G.Y., Thundat, T., Wachter, E.A. & Warmack, R.J. Adsorption-Induced Surface Stress and Its Effects on Resonance Frequency of Microcantilevers. *J. Appl. Phys.* **77,** 3618-3622 (1995).

S12. Lee, J.H., Kim, T.S. & Yoon, K.H. Effect of mass and stress on resonant frequency shift of functionalized Pb(Zr0.52Ti0.48)O-3 thin film microcantilever for the detection of C-reactive protein. *Appl. Phys. Lett.* **84,** 3187-3189 (2004).

S13. Carr, D.W. & Craighead, H.G. Fabrication of nanoelectromechanical systems in single crystal silicon using silicon on insulator substrates and electron beam lithography. *J. Vac. Sci. Technol. B* **15,** 2760-2763 (1997).

S14. Tamayo, J., Pini, V., Gil-Santos, E., Ramos, D., Kosaka, P., Tong, H.D., van Rijn, C. & Calleja, M. Shedding Light on Axial Stress Effect on Resonance Frequencies of Nanocantilevers. *Acs Nano* **5,** 4269-4275 (2011).